JGR Space Physics

RESEARCH ARTICLE
10.1029/2018JA026337

Evaluation of Plasma Properties From Chorus Waves Observed at the Generation Region

Lilla Juhász[1], Yoshiharu Omura[2], János Lichtenberger[1,3], and Reinhard H. Friedel[4]

[1]Department of Geophysics and Space Science, Eötvös University, Budapest, Hungary, [2]Research Institute of Sustainable Humanosphere, Kyoto University, Kyoto, Japan, [3]Research Center for Astronomy and Earth Sciences, Hungarian Academy of Sciences, Sopron, Hungary, [4]Space Science and Applications Group, Los Alamos National Laboratory, Los Alamos, NM, USA

Key Points:
- Linear growth of whistler mode waves forms triggering waves for nonlinear chorus emissions
- We have developed an inversion method to derive energetic electron properties from observation of chorus emissions
- The particle properties derived from chorus inversion agree with energetic particle measurements

Correspondence to:
L. Juhász,
lilla@sas.elte.hu

Citation:
Juhász, L., Omura, Y., Lichtenberger, J., & Friedel, R. H. W. (2019). Evaluation of plasma properties from chorus waves observed at the generation region. *Journal of Geophysical Research: Space Physics*, *124*, 4125–4136. https://doi.org/10.1029/2018JA026337

Received 25 NOV 2018
Accepted 1 MAY 2019
Accepted article online 6 MAY 2019
Published online 14 JUN 2019

Abstract In this study we present an inversion method which provides thermal plasma population parameters from characteristics of chorus emissions only. Our ultimate goal is to apply this method to ground-based data in order to derive the lower-energy boundary condition for many radiation belt models. The first step is to test the chorus inversion method on in situ data of the Van Allen Probes in the generation region. The density and thermal velocity of energetic electrons (few kiloelectron volts to 100 keV) are derived from frequency sweep rate and starting frequencies of chorus emissions through analysis of wave data from the Electric and Magnetic Field Instrument Suite and Integrated Science on board the Van Allen Probes. The nonlinear wave growth theory of Omura and Nunn (2011, https://doi.org/10.1029/2010JA016280) serves as the basis for our inversion method, assuming that the triggering wave is originated by the linear cyclotron instability. We present 16 consecutive rising-tone emissions recorded in the generation region between 11 and 12 UT on 14 November 2012. The results of the inversion are compared with density and thermal velocities (parallel and perpendicular) of energetic electrons derived from the unidirectional flux data of the Helium, Oxygen, Proton, and Electron instrument, showing a good agreement: The normalized root-mean-square deviation between the measured and predicted values are less than ~ 15%. We found that the theoretical amplitudes are consistent with the measured ones. The relation between linear and nonlinear wave growth agrees with our basic assumption; namely, linear growth is a preceding process of nonlinear wave growth. We analyze electron distributions at the relativistic resonant energy ranges.

1. Introduction

In recent years NASA missions such as Time History of Events and Macroscale Interactions during Substorms (THEMIS), Van Allen Probes (RBSP), and Magnetospheric Multiscale advanced our understanding of the complex interconnections of the geospace environment because of the availability of in situ data. Some of these in situ data are the boundary conditions and parametric input to many space environment models and are critical to enable accurate nowcasts and forecast. However, a trusted operational system would rely on continuous and long-running measurements of them. A solution for that need can be ground-based measurements of key parameter inputs. The PLASMON project (PLASmasphere MONitoring, an FP7-SPACE-2010-1 Collaborative Project) is an outstanding example for efforts to produce important key parameters, like plasmasphere densities, with the use of ground-based whistler measurements (Lichtenberger et al., 2013). As part of PLASMON, the global AWDANet network (Automatic Whistler Detector and Analyzer Network, Lichtenberger, 2009; Lichtenberger et al., 2008)—consisting of 28 very low frequency receiver stations—can be extended with the capability of recording whistler mode chorus emissions at stations with magnetic footprint $L > 4(3)$. In particular, we will show in this paper how rising tone chorus emissions can be used as a proxy to estimate the in situ thermal plasma conditions, which form the low-energy boundary condition of many of our current state-of-the-art radiation belt and ring current models.

Coherent chorus emissions are typically observed as rising/falling tones in the frequency range of $0.1f_{ce} < f < 0.8f_{ce}$ with discontinuity at $0.5f_{ce}$, where f_{ce} is the electron gyrofrequency (Burtis & Helliwell, 1969; Koons & Roeder, 1990; Santolík et al., 2003; Sazhin & Hayakawa, 1992) . These emissions are typically excited during geomagnetic storms close to the magnetic equator in low-density plasmas near outside the plasmapause.

Chorus emissions are known to be generated via wave-particle interactions with an anisotropic distribution of energetic electrons (few kiloelectron volts to 100 keV) injected from the plasma sheet (Anderson & Maeda, 1977; Kennel & Petschek, 1966; Li et al., 2013; LeDocq et al., 1998; Meredith et al., 2001; Omura et al., 2009; Santolík et al., 2010; Spasojevic, 2014). Anisotropic angular distributions of substorm injected energetic electrons (also called source population; Jaynes et al., 2015) are able to provide free energy for chorus wave excitation (Thorne et al., 2013, and references therein) and cause isotropic pitch angle distribution in the energy range of the interacting particles. The attention of radiation belt modelers recently turned to whistler mode chorus waves due to its role in both accelerating electrons to megaelectron volts energies in the Earth's outer radiation belt (Horne & Thorne, 1998; Summers et al., 1998, 2002; Li et al., 2014; Reeves et al., 2013; Thorne et al., 2013) and in pitch angle scattering of electrons into the atmospheric loss cone (Hikishima et al., 2010; Lorentzen et al., 2001; O'Brien et al., 2004; Thorne et al., 2005). The generation of chorus emissions is known to be driven by electron cyclotron resonance (Chum et al., 2007; Katoh & Omura, 2007a, 2007b; Kennel & Petschek, 1966; Kennel & Thorne, 1967; Nunn et al., 1997; Omura et al., 2008; Tsurutani & Smith, 1974).

Omura et al. (2008) and Omura and Nunn (2011) proposed a nonlinear wave growth theory for chorus wave generation. They assumed that linear instability excites a coherent whistler mode wave which triggers the nonlinear process. They found a relationship between measurable characteristics (frequency sweep rate $\partial\omega/\partial t$, optimum wave amplitude Ω_{w0}, threshold amplitude Ω_{th}) of rising-tone emissions and the distribution function of energetic electrons (ratio of number densities of hot and cold electrons N_h/N_c and their parallel and perpendicular thermal velocity, $V_{t||}$ and $V_{t\perp}$, respectively) participating in wave-particle interaction. Their theory reveals the amplitude dependency of frequency sweep rate of chorus emissions at the generation region close to the magnetic equator. During quasi-parallel propagation away from the magnetic equator, wave amplitude of chorus emissions undergo a convective growth due to the gradient of the magnetic field, but $\partial\omega/\partial t$ is affected only by cold plasma dispersion. During its slightly oblique propagation away from the equator, the gap at $0.5f_{\mathrm{ce}}$ is formed by nonlinear wave damping via Landau resonance (Hsieh & Omura, 2018).

The above mentioned features of the theory led the AWDANet Team to start to develop a method to derive density and thermal velocities of energetic electrons (source population) from chorus emissions recorded on the ground after they were projected from the ground to the equatorial generation region by a propagation model. In this paper we do not discuss the propagation of chorus emissions, which would lead to a frequency-dependent propagation group delay resulting a different frequency sweep rate. For this study, we selected chorus emissions detected at the assumed generation region (no propagation) and leave the effects of propagation to our follow-up paper. However, it is essential to bear the limitations of ground observations in mind. When we developed our chorus inversion method to monitor the equatorial source population, we took into account that the following data are available on AWDANet stations: (1) electromagnetic wave recordings (fs = 20 kHz), (2) equatorial electron plasma number density from PLASMON, and (3) electron gyrofrequency obtained from a chosen geomagnetic field model via the station's L value. Points (2) and (3) assume that chorus emissions propagate with a group velocity quasi-parallel to the magnetic field.

The main objective of this study is to apply and validate the chorus inversion method, which incorporates the methods of direct comparison of chorus measurements with the nonlinear theory of Foster et al. (2017). The theoretical background of chorus inversion is described in section 2. In the section 3, we present the results of our method on 16 chorus emissions selected from the Electric and Magnetic Field Instrument Suite and Integrated Science (EMFISIS) data of RBSP spacecraft A. Then, we validate the results with simultaneously measured Helium, Oxygen, Proton, and Electron (HOPE) data from the same spacecraft and analyze the theoretical amplitudes and growth rates. To support the validation process, we also analyzed the changes of total electron flux and thermal anisotropies from HOPE and Magnetic Electron Ion Spectrometer (MagEIS) instruments. Section 4 gives a summary and conclusion.

2. Determination of Thermal Velocity and Density of Energetic Electrons

The inversion method consists of two phases (Figure 1). First we estimate the parallel and minimum perpendicular thermal velocity of the source population using the relativistic solution of electromagnetic R-mode wave instability of (Xiao et al., 1998) (first phase blue box in Figure 1). Using these thermal velocities, a direct estimation of N_h/N_c is obtained from the frequency sweep rate of a chorus emission using nonlinear

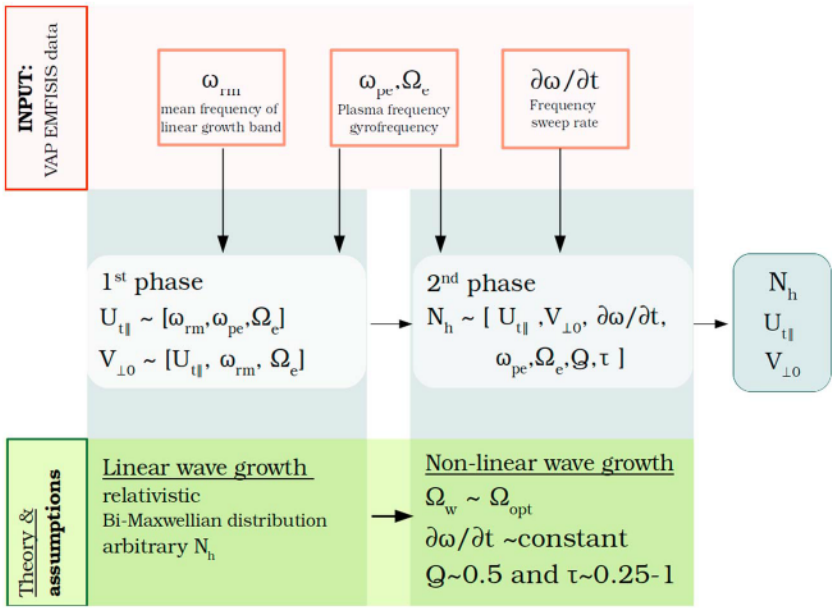

Figure 1. Chorus inversion method: Inputs are from Electric and Magnetic Field Instrument Suite and Integrated Science wave measurements (red boxes) only. As the first step, thermal momentum $U_{t||}$ and average perpendicular velocity $V_{\perp 0}$ are calculated assuming that linear wave growth is the initial phase of chorus generation. The second phase is governed by nonlinear wave growth. Here, we replace the wave amplitude Ω_w with the optimum amplitude Ω_{opt} in order to obtain N_h. For the calculation of N_h, we use the output of the first phase, $U_{t||}$ and $V_{\perp 0}$. At the end of the process, we obtain the bi-Maxwellian function parameters of energetic electrons responsible for chorus emission generation. In the green boxes we note some important assumptions.

wave growth theory (second phase blue box). For this study, the inputs are gyrofrequency Ω_e, plasma frequency ω_{pe}, frequency sweep rate of an individual chorus emission $\partial\omega/\partial t$, and the mean frequency of the assumed band of linear growth ω_{rm}. Nonlinear wave growth—and the accompanying frequency increase—is triggered by the aforesaid hiss-like emission; therefore, its frequency band is lower than the starting frequency of chorus emissions. All data are from EMFISIS measurements (red boxes in Figure 1). More about assumptions (green boxes in Figure 1) is in the descriptions of the theories mentioned above.

2.1. Relativistic Linear Growth Rate of R-Mode Plasma Waves

A band of whistler mode waves is usually present at or below the starting frequency of chorus emissions and acts as a triggering wave for nonlinear wave growth mechanism. This band is assumed to be generated due to relativistic whistler mode instability that is driven by temperature anisotropy of the source population, $A^M = T_\perp/T_{||} - 1 = V_{t\perp}^2/V_{t||}^2 - 1$ in the case of bi-Maxwellian distribution function. The instability of electromagnetic R-mode waves in a relativistic plasma was studied by Xiao et al. (1998). They expressed the linear growth rate as

$$\omega_i = \frac{\pi\omega_{pe}^2\eta_{\text{rel}}}{[2\omega_r + \omega_{pe}^2|\Omega_e|/(\omega_r - |\Omega_e|)^2]}\{A_{\text{rel}} - A_c\}, \tag{1}$$

where η_{rel} is the fraction of the relativistic particle distribution near resonance, which is proportional to the ratio of hot and cold electron density, $N_h/N_c \ll 1$. A_{rel} is the relativistic pitch angle anisotropy of the resonant particles, which in the nonrelativistic limit is equal to A^M. The critical anisotropy is

$$A_c = \frac{1}{\Omega_e/\omega_r - 1}. \tag{2}$$

In their paper, Xiao et al. (1998) evaluated the linear wave growth rate as a function of frequency ω_r, by numerical integration along the resonance ellipse for different distribution functions, and studied the effects of key parameter changes. In the case of bi-Maxwellian distribution, they found that the variation of N_h/N_c only affects the magnitude of the growth rate. Similarly, the increase of A_{rel} is followed by increasing growth rate; in addition, the frequency range of the instability is slightly spreading. Another important key parame-

ter is the ratio of electron plasma and gyrofrequency ω_{pe}/Ω_e: Decreasing ω_{pe}/Ω_e shifts the maximum growth rate to higher frequencies. Likewise, decreasing the hot electron temperature ($U_{t||}$) increases the frequency of the maximum growth rate and also thins the unstable frequency range.

We assume that the linear growth rate takes the maximum value at the mean frequency of whistler instability's wave band ω_{rm}, that frequency is only determined by ω_{pe}/Ω_e and $U_{t||}$. In the chorus inversion ω_{pe}/Ω_e and N_c are known; therefore, those $U_{t||}$ that produce the maximum linear growth rate of the whistler-mode instability at ω_{rm} can be the estimate for initial parallel thermal momentum of the source population. Moreover, the minimum resonant anisotropy required for instability A_c provides the minimum value of $V_{t\perp}$. At this stage of the chorus inversion, we use an arbitrary N_h, because it does not affect the frequency of the maximum growth rate. N_h is calculated in the second step of the chorus inversion method employing the nonlinear wave growth theory.

2.2. Nonlinear Wave Growth Theory

Linear wave growth induces the initial amplitudes of emissions followed by nonlinear wave growth (Omura et al., 2008; Omura & Nunn, 2011) which is responsible for the growing amplitude and rising frequency of chorus emissions assuming parallel propagation at the generation region. Omura et al. (2009) proposed that the formation of gap between the upper and lower bands is due to the nonlinear damping mechanism caused by slightly oblique propagation away from the equator. The frequency sweep rate of chorus emission is derived from the definition of the inhomogeneity ratio of the relativistic second-order resonance condition, and its value is chosen to maximize the magnitude of the resonant current in the direction of the wave electric field at the equator,

$$\frac{\partial\tilde{\omega}}{\partial t} = \frac{0.4 s_0 \omega}{s_1}\tilde{\Omega}_w, \tag{3}$$

where $s_0 = \tilde{V}_{\perp 0}\chi/\xi$, $s_1 = \gamma(1 - \tilde{V}_R/\tilde{V}_g)^2$, $\tilde{\Omega}_w = eB_w/(m_0\Omega_{e0})$, and $\tilde{\omega} = \omega/\Omega_{e0}$ is the normalized frequency. B_w is the wave magnetic field; $\chi^2 = (1+\xi^2)^{-1}$ and $\xi^2 = \omega(\Omega_e - \omega)/\omega_{pe}^2$; and $\tilde{V}_g$ is the group velocity normalized by the speed of light c. $\tilde{V}_{\perp 0}$ is the averaged perpendicular velocity of the source population. It should be noted that the relation between frequency sweep rate and the wave amplitude has also been recently mentioned by Demekhov et al. (2017) based on the theory of Trakhtengerts et al. (2004). The first-order cyclotron resonance condition provides the resonance velocity,

$$\tilde{V}_R = \chi\xi(\omega - \Omega_e/\gamma) = \frac{\tilde{\omega}^2 - \sqrt{\tilde{\omega}^4 + (\tilde{\omega}^2 + \tilde{V}_p^2)(1 - \tilde{\omega}^2 - \tilde{V}_{\perp 0}^2)}}{\tilde{\omega}^2 + \tilde{V}_p^2}\tilde{V}_p. \tag{4}$$

$\tilde{V}_R$ is dependent upon $V_{\perp 0}$, because we expressed the Lorentz-factor as $\gamma = [1 - (V_R^2 + V_{\perp 0}^2)/c^2]^{-1/2}$. $\tilde{V}_p = V_p/c$ is the phase velocity.

Omura and Nunn (2011) found that the frequency change of a rising-tone chorus is due to the nonlinear correction term in the cold plasma dispersion relation, which is proportional to the component of the resonant current parallel to the wave magnetic field, J_B. This gradual deviation in frequency can exist when the triggering wave amplitude is close to the optimum wave amplitude:

$$\tilde{\Omega}_{w0} = 0.81\pi^{-5/2}\frac{Q}{\tau}\frac{s_1\tilde{V}_g}{s_0\tilde{\omega}\tilde{U}_{t||}}\left(\frac{\tilde{\omega}_{ph}\tilde{V}_{\perp 0}\chi}{\gamma}\right)^2 \exp\left(-\frac{\gamma^2\tilde{V}_R^2}{2\tilde{U}_{t||}^2}\right), \tag{5}$$

where Q represents the depth of electron hole with typical value 0.5. $\tau = T_N/T_{tr}$ is the ratio of nonlinear transition time and nonlinear trapping period, where T_N represents the time required for the formation of nonlinear current. Typical range of $\tau = 0.25 - 1$ is concluded from theory (Omura & Nunn, 2011), simulation (Hikishima & Omura, 2012), and observation (Kurita et al., 2012). $\tilde{U}_{t||} = U_{t||}/c$ is the parallel thermal momentum of the source population.

The threshold amplitude for the amplification of a chorus element is derived from the consideration that the temporal growth rate should be positive at the equator (Omura et al., 2009). Waves can only grow when the optimum amplitude is higher than the threshold amplitude and the triggering wave amplitude exceeds the threshold amplitude,

$$\tilde{\Omega}_{th} = \frac{100\pi^3\gamma^3\xi}{\tilde{\omega}\tilde{\omega}_{ph}^4\tilde{V}_{\perp 0}^5\chi^5}\left(\frac{\tilde{a}s_2\tilde{U}_{t\parallel}}{Q}\right)^2 \exp\left(\frac{\gamma^2\tilde{V}_R^2}{\tilde{U}_{t\parallel}^2}\right), \tag{6}$$

where $s_2 = \frac{1}{2\xi\chi}\left\{\frac{\gamma\omega}{\Omega_e}\left(\frac{V_{\perp 0}}{c}\right)^2 - \left[2+\Lambda\frac{\chi^2(\Omega_e-\gamma\omega)}{\Omega_e-\omega}\right]\frac{V_R V_p}{c^2}\right\}$ is the coefficient related to the gradient of magnetic field in the inhomogeneity ratio (equation (10) of Omura et al., 2009); $\tilde{a} = ac^2/\Omega_{e0} = 4.5c^2/(LR_E\Omega_{e0})$ is the scale length of the dipole magnetic field. $\Lambda = \omega/\Omega_e$ for inhomogeneous electron density model (Λ=1 for constant electron density model).

The nonlinear wave growth is

$$\Gamma_N = \frac{Q\omega_{ph}^2}{2}\left(\frac{\zeta}{\Omega_w\omega}\right)^{1/2}\frac{V_g}{U_{t\parallel}}\left(\frac{V_{\perp 0}\chi}{c\pi\gamma}\right)\exp\left(-\frac{\gamma^2V_R^2}{2U_{t\parallel}^2}\right). \tag{7}$$

To estimate the energetic electron density, we replace the wave amplitude in equation (3) with the optimum wave amplitude (5):

$$\tilde{\omega}_{ph} = \omega_{pe}\left(\frac{N_h}{N_c}\right)^{1/2} = \sqrt{\frac{\partial\omega}{\partial t}\frac{\pi^{5/2}\tau}{0.324Q}\frac{\tilde{U}_{t\parallel}}{\tilde{V}_g}\exp\left(\frac{\gamma^2\tilde{V}_R^2}{2\tilde{U}_{t\parallel}^2}\right)}\frac{\gamma}{\tilde{V}_{\perp 0}\chi}, \tag{8}$$

giving an upper bound of N_h. In the case of known thermal velocities, the number density of the source population N_h can be derived from $\partial\omega/\partial t$. The relativistic linear growth rate theory provides the estimate of $\tilde{U}_{t\parallel}$ and the average perpendicular velocity $V_{0\perp} = \sqrt{\pi/2}V_{t\perp}/c$, where we assume the bi-Maxwellian distribution.

3. Discussion

3.1. Case Studies From EMFISIS Data

On 14 November 2012, the impact of a geomagnetic storm with a minimum $Dst \sim -108$ nT was observable on RBSP A measurements. Chorus emissions were measured by RBSP A EMFISIS instrument from 10 to 13 UT (see Figure 5 a) . (Santolík et al., 2014, analyzed the fine structures of chorus emissions in the consequent time period, 12–15 UT.) We have selected 16 full, strong chorus emissions from EMFISIS continuous burst mode wave data (28.6-μs time resolution and ~ 12-kHz maximum observable frequency; Kletzing et al., 2013) between 11 and 12 UT. The RBSP spacecraft A was close to the plasmapause (L = 5.42–5.87) in the dawn sector (MLT = 4.92–5.61) and crossed the magnetic equator (mlat = 0.755–(−0.649)°).

At that time, the gap at half the gyrofrequency was not formed clearly, and relatively small number of emissions existed. Therefore, we concluded that (a) the satellite was at the generation region and (b) wave-particle interaction corresponding to the small number of emissions did not affect significantly the particle distribution of the source population . In Figure 2a, three series of rising-tone emissions with large-amplitude ~ 0.1–0.5 nT are shown. The multicomponent wave measurement allows us to estimate the angle between the direction of propagation and the background magnetic field θ and the ellipticity and planarity of these emissions by the singular value decomposition method (Santolík et al., 2003). The waves exhibit quasi-parallel propagation (Figure 2b), high coherence (Figure 2c), and right-hand polarization (Figure 2d). We present our method through the analysis of the three events in Figure 3.

To estimate the parallel and minimum perpendicular thermal velocities, first we identify the band of whistler-mode waves corresponding to the linear wave growth. The lower and upper limits of these bands are 790–1,200, 790–1,265, and 820–1,130 Hz, respectively, indicated by white dashed lines in Figure 2a from left to right. From EMFISIS measurement (Kurth et al., 2015) we obtain $\omega_{pe}/\Omega_e \sim 5.17$, 5.46, and 5.41, respectively. Assuming arbitrary N_h, we search for $U_{t\parallel}$ value that produces the maximum linear growth rate at the mean frequency of the linear wave growth band ω_{rm}. In the knowledge of $U_{t\parallel}$, a minimum estimate for $V_{\perp 0}$ can be calculated from (2) and

$$A_c = \frac{V_{t\perp}^2}{V_{t\parallel}^2} - 1 = \frac{(V_{\perp 0}/\sqrt{\frac{\pi}{2}})^2}{(U_{t\parallel}/\gamma_R)^2} - 1. \tag{9}$$

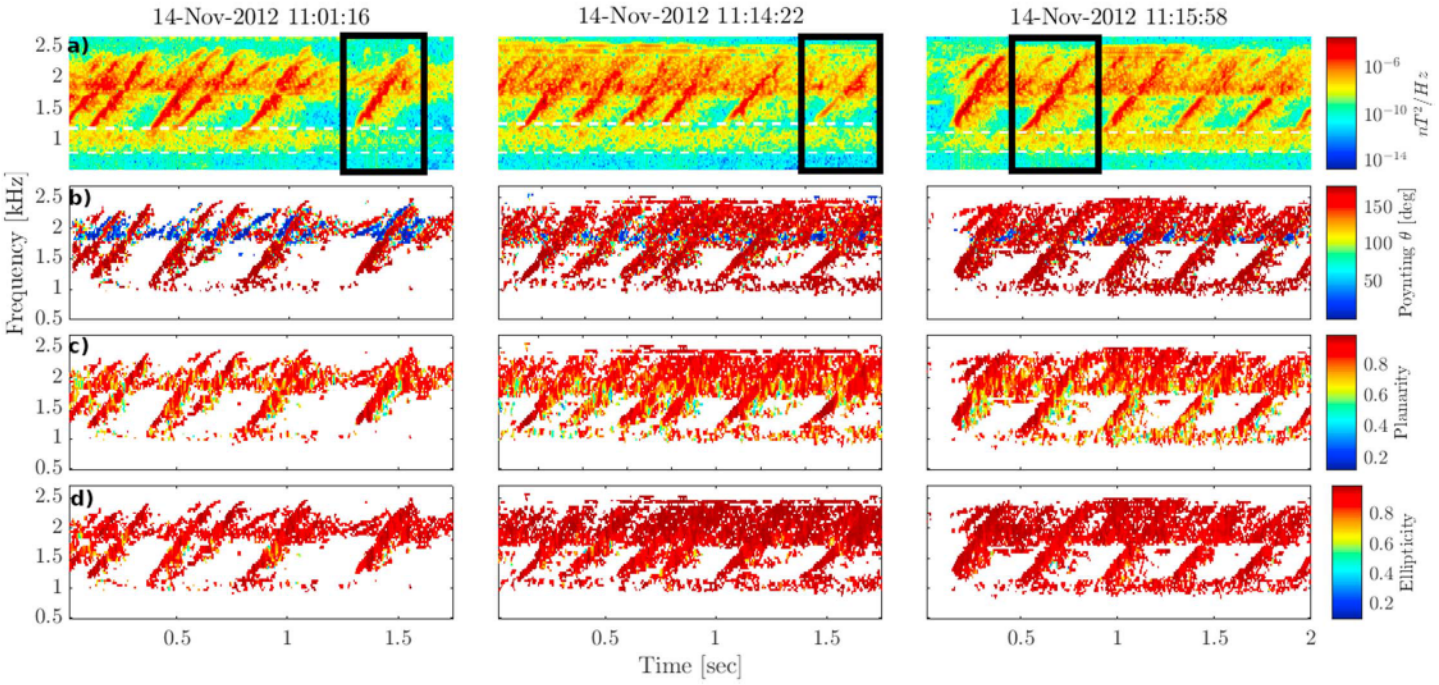

Figure 2. Van Allen Probes Electric and Magnetic Field Instrument Suite and Integrated Science-A burst data recorded on 14 November 2012, 11:01:16.67 UT (first column), 11:14:22.67 UT (second column), and 11:15:58.67 UT (third column). (a) Spectrogram of single-axis (BuBu) magnetic field. White dashed lines contour the assumed band of linear wave growth. (b) Poynting vector angle θ with respect to the background geomagnetic field B_0. (c) Planarity and (d) ellipticity (magnetic power spectral density, is greater than $\sim 10^7$ nT^2/Hz). Black rectangles indicate the emissions we analyze in detail in section 3.

In Figure 3, we present the results of three emissions selected from Figure 2, plotting frequency sweep rates, amplitudes, and growth rates. The top row of plots presents the spectrogram, instantaneous frequency (blue lines), and fitted curves (dashed white lines) of rising-tone emissions. We obtain the instantaneous frequencies of chorus emissions at the zero crossings of the wave magnetic field's perpendicular component with respect to the background magnetic field. The relation between measured (yellow solid lines) and theoretical amplitudes are plotted in the middle row of Figure 3: optimum wave amplitudes (blue lines) are in the same order as the measured amplitudes and have higher value than threshold amplitude (red solid and dashed lines). Moreover, the observed amplitudes start to grow when they exceed the threshold amplitude. The nonlinear chorus generation is always triggered by an existing wave, and we assumed that they start through linear wave-particle interaction. The nonlinear wave growth takes over when the wave amplitude exceeds the threshold amplitude. The nonlinear wave growth carries on, and the procedure is stabilized when the amplitude reaches the optimum wave amplitude. These transitions take place within finite time interval; this is why the amplitude is lower than the optimal one at the beginning of the excitation process. Although we used $\tau = 0.25$ and 0.5 for chorus inversion, the optimum amplitude is the same, because a constant value of $\partial\omega/\partial t$ determines the product of τ and N_h/N_c. Threshold amplitude is the function of N_h/N_c, which changes with τ. Therefore, using $\tau = 0.5$ and 0.25 yields a lower (red solid line) and upper (red dashed line) estimate of the threshold amplitude. The optimum amplitude of the 14 November 2012, 11:14:24.570 UT event slightly differs from the measured one at higher frequencies: It can be due to overlapping, separate upper-band chorus emissions or convective growth. In the bottom row, yellow dashed lines represent ω_{rm} as they cross the linear growth rate curve (dashed red lines) at the maximum. Nonlinear growth rate (blue solid [$\tau = 0.5$] and dashed [$\tau = 0.25$] lines) is higher than linear growth rate, as it was proposed by Summers et al. (2013). The frequency range of the linear instability is confined to $\sim$ 500–1,500 Hz. (We used $\tau = 0.25$–0.5 instead of 0.25–1 in these plots; because the values of nonlinear growth rate corresponding to $\tau = 1$ are almost 2 orders higher than linear growth rates, it is difficult to show the changes of the latter one in the plot.)

The method of chorus inversion is sensitive to the value of ω_{rm}. To obtain the standard deviation of thermal velocities, the frequencies of lower and upper edge of the band are used. In Figure 4, $V_{t||}$ (middle panel) and $V_{t\perp}$ (bottom panel) of the 16 chorus elements are marked with the squares in the middle of the red bars,

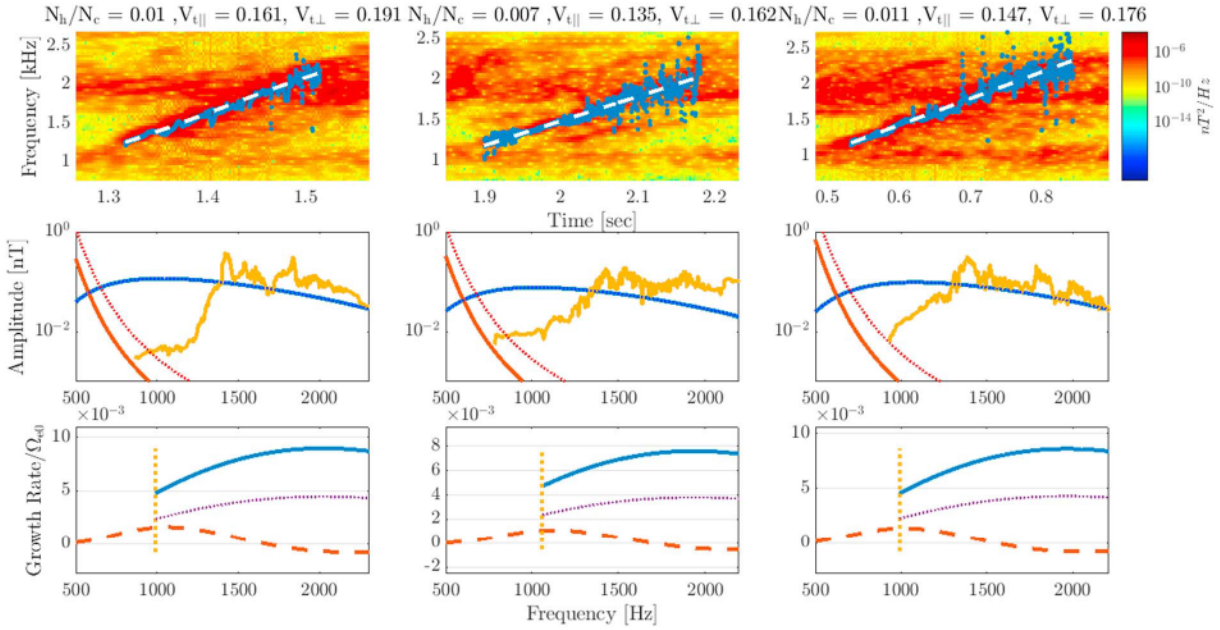

Figure 3. Chorus emissions from 14 November 2012, 11:01:17.986 UT (left column), 14 November 2012, 11:14:24.570 UT (middle column), and 14 November 2012, 11:15:59.202 UT (right column). (top row) The spectrogram, instantaneous frequency (blue lines), and the linear approximation (dashed white lines) of the emissions. The optimum amplitudes (middle row, blue lines) are of the same order as the measured amplitude (yellow lines) and are not affected by the change of τ. Threshold amplitudes of $\tau = 0.5$ and 0.25 are plotted by solid and dotted red lines, respectively. The threshold amplitude does not depend on τ directly. However, changes of τ modify N_h/N_c, which affects the threshold amplitude. (bottom row) Linear growth rate (dashed red line) and w_{rm} (yellow dashed lines). Nonlinear wave growth rates are plotted by blue solid ($\tau = 0.5$) and dotted ($\tau = 0.25$) lines.

and the vertical extents of the bars represent the standard deviations of $V_{t||}$ and $V_{t\perp}$. The magnitude of the standard deviation depends on the width of the linear growth rate band. As the second step, we use the instantaneous frequencies of chorus emissions. Assuming that the frequency of the main part of the chorus emissions is a linear function of time, we can approximate the frequency sweep rate $\partial\omega/\partial t$ with a constant value.

When the derived values of $U_{t||}$, $V_{\perp 0}$, and $\partial\omega/\partial t$ are substituted into (8), N_h/N_c can be calculated directly. Note that the replacement of wave amplitude with optimum amplitude leads to an upper estimate of N_h/N_c. As we already mentioned, the ratio of nonlinear transition time and nonlinear trapping period τ could be between 0.25 and 1; this provides an interval for N_h/N_c. In the top panel of Figure 4, N_h/N_c, corresponding to $\tau = 0.25$–1, is shown with red error bars and is typically between 0.002 and 0.012. The red square in the middle of the error bars corresponds to $\tau = 0.73$, which is the best fit to HOPE data (blue error bars).

3.2. Comparison of Results of the Inversion and In Situ Measurements (HOPE Data)

The HOPE Mass Spectrometer (Funsten et al., 2013) measures the fluxes of electrons and dominant ion species in the energy range of 1 eV to 50 keV, in 36 logarithmically spaced steps (before September 2013) that were later modified to 72 log-spaced steps, at an energy resolution $\Delta E_{\mathrm{FWHM}}/E \approx 0.15$. The $4sr$ field of view is attained by five polar pixels (consisting of individual detectors) and the spin of the spacecrafts; however, HOPE data sampling is not spin synchronized. As a result, electron flux data are available as a function of energy and pitch angle. In this section, we compare the output of the inversion $[N_h, U_{t||}, V_{\perp 0}]$ with those derived from HOPE measurements, based on the following equations (Wu et al., 2013; Goldstein et al., 2014):

$$N_h^* = 2\pi \int_0^{\pi} \int_{v_{\min}}^{v_{\max}} f(v,\alpha) v^2 \mathrm{d}v \sin\alpha \mathrm{d}\alpha \approx 2\pi \sum_j \sum_i J_{ij} \left(\frac{2E_i}{m_e}\right)^{-1/2} \sin\alpha_j \mathrm{d}E_i \mathrm{d}\alpha_j, \tag{10}$$

$$V_{t||}^{*2} = \frac{2\pi}{3N_h} \int_0^{\pi} \int_{v_{\min}}^{v_{\max}} v^2 (\cos\alpha)^2 f(v,\alpha) v^2 \mathrm{d}v \sin\alpha \mathrm{d}\alpha$$
$$\approx \sqrt{\frac{2\pi^2}{m_e}} \frac{1}{3N_h} \sum_j \sum_i J_{ij} (E_i)^{1/2} \sin\alpha_j \cos^2\alpha_j \mathrm{d}E_i \mathrm{d}\alpha_j, \tag{11}$$

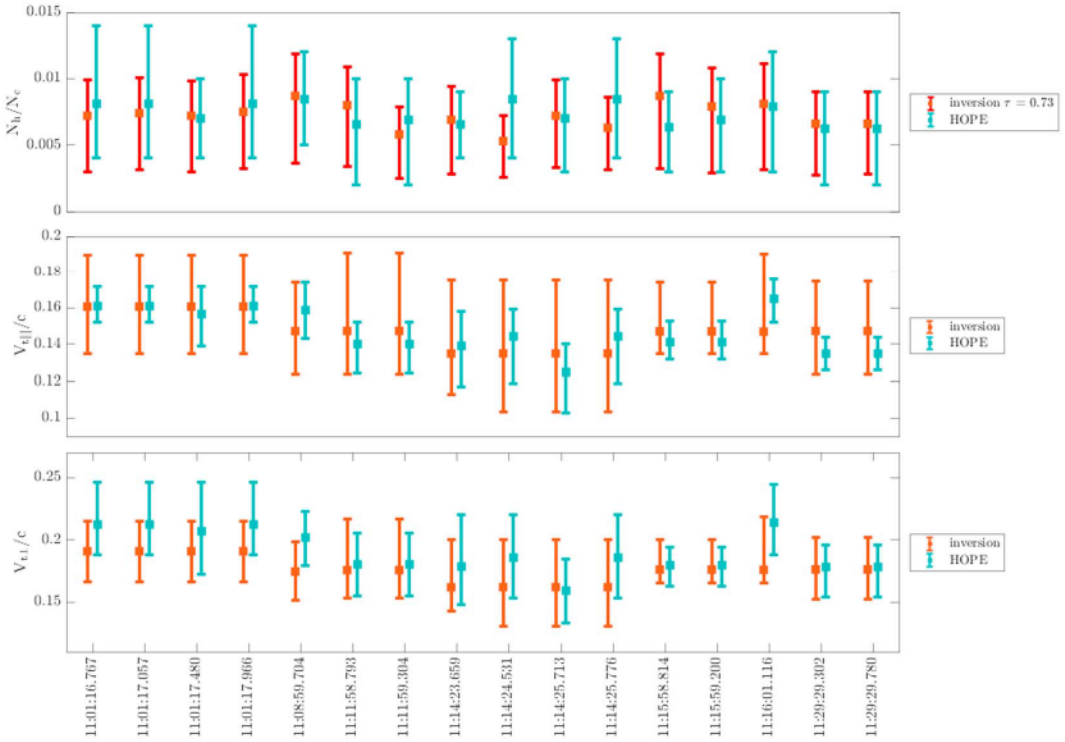

Figure 4. Results of the chorus inversion of the selected 16 chorus emissions (referred to by their date). N_h/N_c obtained from HOPE measurements are shown with blue error bars. The result of the inversion for N_h/N_c is a range (red) given by the minimum and maximum values of this interval corresponding to $\tau = 0.25$ and 1, respectively. (top panel) The best fit of $\tau = 0.73$ of the inversion to HOPE measurements with red squares. (middle and bottom panel) Parallel and minimum estimate of perpendicular thermal velocities from the inversion (red) and HOPE (blue) with error bars. HOPE = Helium Oxygen Proton Electron instrument.

$$V_{t\perp}^{*2} = \frac{\pi}{3N_h}\int_0^{\pi}\int_{v_{min}}^{v_{max}} v^2(\sin\alpha)^2 f(v,\alpha)v^2 \mathrm{d}v\sin\alpha\mathrm{d}\alpha$$
$$\approx \sqrt{\frac{\pi^2}{2m_e}}\frac{1}{3N_h}\sum_j\sum_i J_{ij}(E_i)^{1/2}\sin\alpha_j\sin^2\alpha_j \mathrm{d}E_i\mathrm{d}\alpha_j, \quad (12)$$

where N_h^*, $V_{t||}^*$, and $V_{t\perp}^*$ are the hot electron density and parallel and perpendicular velocities from HOPE measurements. $f(v,\alpha)$ is the hot electron distribution function in the velocity v and pitch angle α space. This theoretical description is substituted with measurable quantities such as flux J, mean energy E, and energy width dE_i of the specific energy channel. Indices i,j represent the given energy channels and pitch angle bin.

To identify the highest and lowest energy channel of the instrument corresponding to the relativistic resonance energy of given chorus emissions, namely $[v_{min}, v_{max}]$, we employ the expression of Lorentz-factor from Xiao et al. (1998):

$$\gamma_R = \frac{-1+(ck/\omega_r)[\{(ck/\omega_r)^2-1\}(1+u_\perp^2/c^2)(\omega_r/\Omega_e)^2+1]}{\{(ck/\omega_r)^2-1\}(\omega_r/\Omega_e)}, \quad (13)$$

where k is the wavenumber and $u_\perp$ is the perpendicular momentum. Here, we substitute the lowest and half-gyrofrequency value of each chorus emission to ω_r, and replace $u_{t\perp}$ with the average value of perpendicular momentum derived from critical anisotropy and parallel thermal momentum. (Note that the use of equation (4) gives almost identical result.) The energy range of the comparison is based on the lower band of the selected chorus emissions.

To determine the standard deviation of N_h^*, $V_{t||}^*$, and $V_{t\perp}^*$, we consider the neighboring energy channels of lowest and highest energy channels, altogether six channels, and we use all combinations (nine) to pick up the minimum, maximum, and mean values.

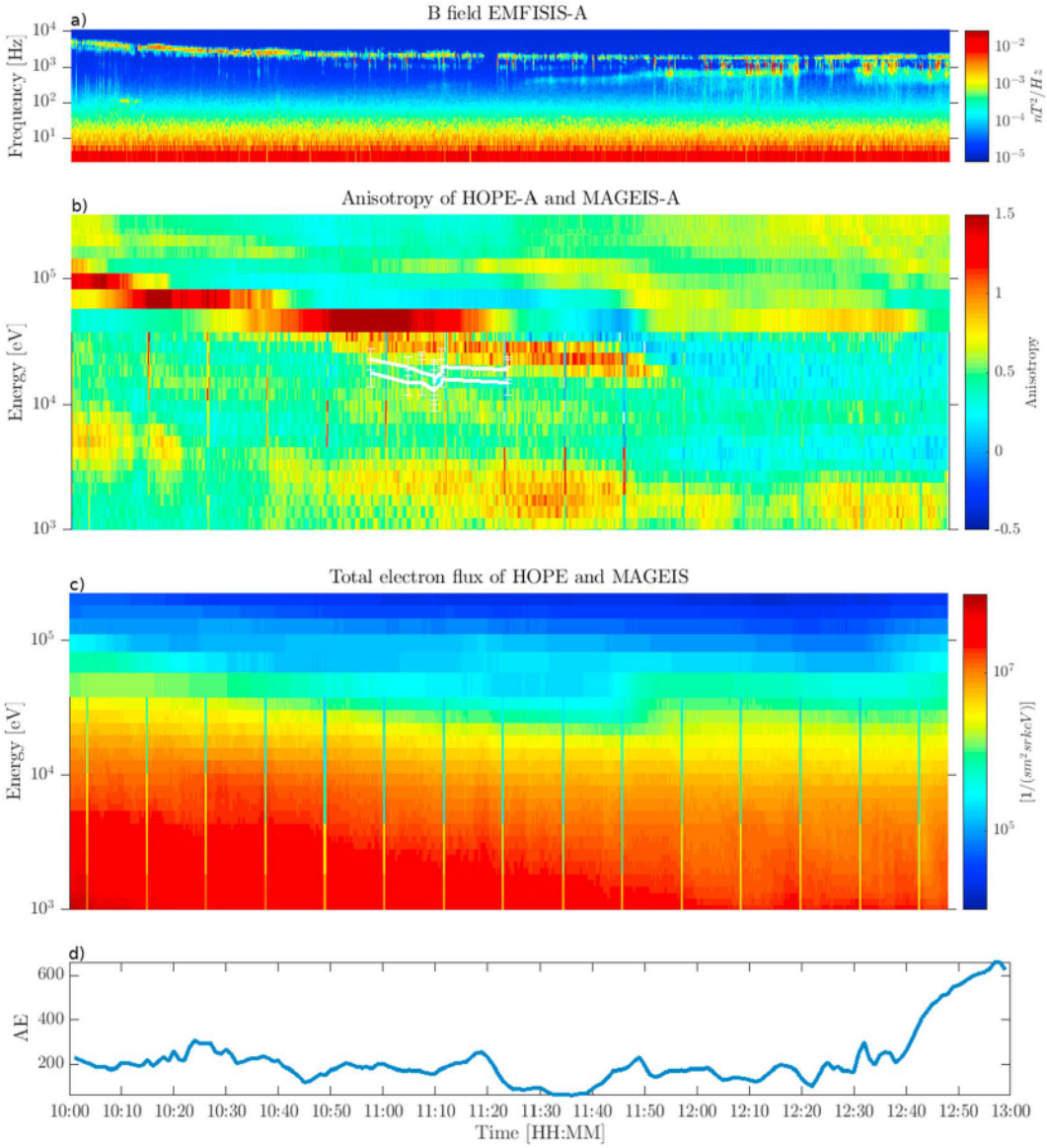

Figure 5. (a) Spectrogram of single-axis (BuBu) magnetic field (top panel) measured by Electric and Magnetic Field Instrument Suite and Integrated Science on board Van Allen Probes spacecraft A between 10 and 13 UT on 14 November 2012. (b) Pitch angle anisotropy map derived from HOPE-A and MAGEIS-A measurements with resonance energy ranges of the analyzed cases (white lines). (c) Total electron fluxes measured by HOPE-A and MAGEIS-A (top panel). (d) *AE* index. HOPE = Helium Oxygen Proton Electron instrument; MagEIS = Magnetic Electron Ion Spectrometer.

The results of $N_h/N_c{}^*$, $V^*_{t||}$, and $V^*_{t\perp}$ derived from HOPE measurements are plotted with light blue squares in Figure 4; the error bars show the standard deviation. N_h/N^*_c values derived from HOPE measurements (blue) are in the range of N_h/N_c (red error bars) corresponding to $\tau = 0.25$ and 1 . The normalized root-mean-square deviation between the HOPE (N_h/N^*_c, $V^*_{t||}$, and $V^*_{t\perp}$) and the theoretical (N_h/N_c, $V_{t||}$, and $V_{t\perp}$) values are $N_h/N_{c\mathrm{NRMS}} \sim 0.13$, $V_{t||\mathrm{NRMS}} \sim 0.06$, and $V_{t\perp\mathrm{NRMS}} \sim 0.1$, respectively.

To affirm our results, we further analyzed anisotropy (Figure 5b), omnidirectional flux (Figure 5c), *AE* index (Figure 5d), and wave magnetic data (Figure 5a) in a longer timescale of 10–13 UT. During this time interval, the spacecraft was flying away from the Earth to higher L shells (4–6) and was moving from the nightside to the morning sector MLT = 4–6. The pitch angle anisotropy map in the second panel is calculated by the method of Chen et al. (1999) using both HOPE-A (few electron volts to 50 keV) and MAGEIS-A (15–224 keV) particle flux measurements. This method allows us to perform a least squares fit to the observed pitch angle

distributions for a fixed kinetic energy, then calculate the anisotropy from the adjustable parameters of that function. The anisotropy map shows two strong anisotropic bands; one starts at 100 keV and ends at ~ 35 keV at 10:55UT, and the other starts below 10 keV and runs parallel with the previous one. In our interpretation these anisotropic bands are the result of an injection from the plasma sheet, and the plasma was accelerated in a convective transport from the nightside to the dayside. The more isotropic region between the two bands is presumably due to wave-particle interaction between electrons in this energy range and chorus emissions (see top panel). This explanation agrees with the resonance energy ranges of the analyzed chorus emissions: the upper white line corresponds to the starting frequency of these emissions, the lower one corresponds to half the gyrofrequency.

4. Summary and Conclusion

A new method is presented to derive N_h, $V_{t||}$, and $V_{t\perp}$ from the EMFISIS wave measurement *only*. To extract these parameters from the wave data, we assumed that (a) the frequency sweep rate of the chorus elements is proportional to the optimum wave amplitude, (b) the optimum wave amplitude is proportional to the ratio of density of energetic electrons and cold electron density, and (c) the nonlinear wave growth generation is anticipated by linear growth rate, which is present on the dynamic spectra as a band of whistler-mode waves close to the starting frequency of chorus emissions in our cases. Sixteen strong chorus emissions close to the generation region (magnetic equator) were analyzed. The output data of chorus inversion N_h, $V_{t||}$, and $V_{t\perp}$ were compared with the same quantities derived from the HOPE measurements in the energy range of the relativistic resonance of the selected chorus emissions, showing a good agreement ($N_h/N_{\mathrm{cNRMS}} \sim 0.13$, $V_{t||\mathrm{NRMS}} \sim 0.06$, and $V_{t\perp\mathrm{NRMS}} \sim 0.1$). The measured amplitudes are consistent with the optimum and threshold amplitudes of nonlinear wave growth theory; the nonlinear growth rate has positive values in the entire frequency range of chorus emissions, contrary to the prediction of the linear growth rate theory. In the next step, the method presented here will be extended with chorus emissions recorded on the ground, replacing the in situ wave measurements. This extension requires a suitable chorus propagation model. This way, the density of the energetic electrons can be estimated from ground data, forming a new complement or a stand-alone source of these important data (energetic electron density and parallel and perpendicular thermal velocities: N_h, $V_{t||}$, and $V_{t\perp}$).

Acknowledgments
The research leading to these results received funding from the Hungarian National Research, Development and Innovation Office under grant agreements NN116408 and NN116446. This work was also supported by JSPS KAKENHI grants 15H05815 and 17H06140. This research was supported by the Los Alamos Space Weather Summer School, funded by the Center for Space and Earth Sciences at Los Alamos National Laboratory. Processing and analysis of the HOPE data was supported by Energetic Particle, Composition, and Thermal Plasma (RBSP-ECT) investigation funded under NASA's Prime contract NAS5-01072. All RBSP-ECT data are publicly available at the Web site (http://www.RBSP-ect.lanl.gov/). All RBSP-EMFISIS data used in this paper are available from the Web site (http://emfisis.physics.uiowa.edu/). The research at University of Iowa was supported under NASA Prime contract NAS5-01072.

References

Anderson, R. R., & Maeda, K. (1977). VLF emissions associated with enhanced magnetospheric electrons. *Journal of Geophysical Research*, *82*(1), 135–146.

Burtis, W. J., & Helliwell, R. A. (1969). Banded chorus—A new type of VLF radiation observed in the magnetosphere by OGO 1 and OGO 3. *Journal of Geophysical Research*, *74*(11), 3002–3010. https://doi.org/10.1029/JA074i011p03002

Chen, M. W., Roeder, J. L., Fennell, J. F., Lyons, L. R., Lambour, R. L., & Schulz, M. (1999). Proton ring current pitch angle distributions: Comparison of simulations with CRRES observations. *Journal of Geophysical Research*, *104*(A8), 17379–17389. https://doi.org/10.1029/1999JA900142

Chum, J., Santolík, O., Breneman, A., Kletzing, C., Gurnett, D., & Pickett, J. (2007). Chorus source properties that produce time shifts and frequency range differences observed on different Cluster spacecraft. *Journal of Geophysical Research*, *112*, A06206. https://doi.org/10.1029/2006JA012061

Demekhov, A. G., Taubenschuss, U., & Santolk, O. (2017). Simulation of VLF chorus emissions in the magnetosphere and comparison with THEMIS spacecraft data. *Journal of Geophysical Research: Space Physics*, *122*, 166–184. https://doi.org/10.1002/2016JA023057

Foster, J. C., Erickson, P. J., Omura, Y., Baker, D. N., Kletzing, C. A., & Claudepierre, S. G. (2017). Van Allen Probes observations of prompt MeV radiation belt electron acceleration in nonlinear interactions with VLF chorus. *Journal of Geophysical Research: Space Physics*, *122*, 324–339. https://doi.org/10.1002/2016JA023429

Funsten, H. O., Skoug, R. M., Guthrie, A. A., MacDonald, E. A., Baldonado, J. R., Harper, R. W., et al. (2013). Helium, Oxygen, Proton, and Electron (HOPE) mass spectrometer for the Radiation Belt Storm Probes mission. *Space Science Reviews*, *179*(1), 423–484. https://doi.org/10.1007/s11214-013-9968-7

Goldstein, J., Pascuale, S. D., Kletzing, C., Kurth, W., Genestreti, K. J., Skoug, R. M., et al. (2014). Simulation of Van Allen Probes plasmapause encounters. *Journal of Geophysical Research: Space Physics*, *119*, 7464–7484. https://doi.org/10.1002/2014JA020252

Hikishima, M., & Omura, Y. (2012). Particle simulations of whistler-mode rising-tone emissions triggered by waves with different amplitudes, *117*, A04226. https://doi.org/10.1029/2011JA017428

Hikishima, M., Omura, Y., & Summers, D. (2010). Microburst precipitation of energetic electrons associated with chorus wave generation. *Geophysical Research Letters*, *37*, L07103. https://doi.org/10.1029/2010GL042678

Horne, R. B., & Thorne, R. M. (1998). Potential waves for relativistic electron scattering and stochastic acceleration during magnetic storms. *Geophysical Research Letters*, *25*(15), 3011–3014.

Hsieh, Y. K., & Omura, Y. (2018). Nonlinear damping of oblique whistler mode waves via Landau resonance. *Journal of Geophysical Research: Space Physics*, *123*, 7462–7472. https://doi.org/10.1029/2018JA025848

Jaynes, A. N., Baker, D. N., Singer, H. J., Rodriguez, J. V., Loto'aniu, T. M., Ali, A. F., et al. (2015). Source and seed populations for relativistic electrons: Their roles in radiation belt changes. *Journal of Geophysical Research: Space Physics*, *120*, 7240–7254. https://doi.org/10.1002/2015JA021234

Katoh, Y., & Omura, Y. (2007a). Computer simulation of chorus wave generation in the Earth's inner magnetosphere. *Geophysical Research Letters*, *34*, L03102. https://doi.org/10.1029/2006GL028594

Katoh, Y., & Omura, Y. (2007b). Relativistic particle acceleration in the process of whistler-mode chorus wave generation. *Geophysical Research Letters*, *34*, L13102. https://doi.org/10.1029/2007GL029758

Kennel, C. F., & Petschek, H. (1966). Limit on stably trapped particle fluxes. *Journal of Geophysical Research*, *71*(1), 1–28.

Kennel, C. F., & Thorne, R. M. (1967). Unstable growth of unducted whistlers propagating at an angle to the geomagnetic field. *Journal of Geophysical Research*, *72*(3), 871–878.

Kletzing, C. A., Kurth, W. S., Acuna, M., MacDowall, R. J., Torbert, R. B., Averkamp, T., et al. (2013). The Electric and Magnetic Field Instrument Suite and Integrated Science (EMFISIS) on RBSP, 127–181. https://doi.org/10.1007/s11214-013-9993-6

Koons, H., & Roeder, J. (1990). A survey of equatorial magnetospheric wave activity between 5 and 8 R_E. *Planetary and Space Science*, *38*(10), 1335–1341. https://doi.org/10.1016/0032-0633(90)90136-E

Kurita, S., Katoh, Y., Omura, Y., Angelopoulos, V., Cully, C. M., Le Contel, O., & Misawa, H. (2012). THEMIS observation of chorus elements without a gap at half the gyrofrequency. *Journal of Geophysical Research*, *117*, A11223. https://doi.org/10.1029/2012JA018076

Kurth, W. S., De Pascuale, S., Faden, J. B., Kletzing, C. A., Hospodarsky, G. B., Thaller, S., & Wygant, J. R. (2015). Electron densities inferred from plasma wave spectra obtained by the Waves instrument on Van Allen Probes. *Journal of Geophysical Research: Space Physics*, *120*, 904–914. https://doi.org/10.1002/2014JA020857

LeDocq, M., Gurnett, D., & Hospodarsky, G. (1998). Chorus source locations from VLF Poynting flux measurements with the Polar spacecraft. *Geophysical Research Letters*, *25*(21), 4063–4066.

Li, W., Bortnik, J., Thorne, R., Cully, C., Chen, L., Angelopoulos, V., et al. (2013). Characteristics of the Poynting flux and wave normal vectors of whistler-mode waves observed on THEMIS. *Journal of Geophysical Research: Space Physics*, *118*, 1461–1471. https://doi.org/10.1002/jgra.50176

Li, W., Thorne, R., Ma, Q., Ni, B., Bortnik, J., Baker, D., et al. (2014). Radiation belt electron acceleration by chorus waves during the 17 March 2013 storm. *Journal of Geophysical Research: Space Physics*, *119*, 4681–4693. https://doi.org/10.1002/2014JA019945

Lichtenberger, J. (2009). A new whistler inversion method. *Journal of Geophysical Research*, *114*, A07222. https://doi.org/10.1029/2008JA013799

Lichtenberger, J., Clilverd, M. A., Heilig, B., Vellante, M., Manninen, J., Rodger, C. J., et al. (2013). The plasmasphere during a space weather event: First results from the PLASMON project. *Journal of Space Weather and Space Climate*, *3*, A23.

Lichtenberger, J., Ferencz, C., Bodnár, L., Hamar, D., & Steinbach, P. (2008). Automatic whistler detector and analyzer system: Automatic whistler detector. *Journal of Geophysical Research*, *113*, A12201. https://doi.org/10.1029/2008JA013467

Lorentzen, K., Blake, J., Inan, U., & Bortnik, J. (2001). Observations of relativistic electron microbursts in association with VLF chorus. *Journal of Geophysical Research*, *106*(A4), 6017–6027.

Meredith, N. P., Horne, R. B., & Anderson, R. R. (2001). Substorm dependence of chorus amplitudes: Implications for the acceleration of electrons to relativistic energies. *Journal of Geophysical Research*, *106*(A7), 13165–13178.

Nunn, D., Omura, Y., Matsumoto, H., Nagano, I., & Yagitani, S. (1997). The numerical simulation of VLF chorus and discrete emissions observed on the Geotail satellite using a Vlasov code. *Journal of Geophysical Research*, *102*(A12), 27083–27097.

O'Brien, T., Looper, M., & Blake, J. (2004). Quantification of relativistic electron microburst losses during the GEM storms. *Geophysical Research Letters*, *31*, 04802. https://doi.org/10.1029/2003GL018621

Omura, Y., Hikishima, M., Katoh, Y., Summers, D., & Yagitani, S. (2009). Nonlinear mechanisms of lower-band and upper-band VLF chorus emissions in the magnetosphere. *Journal of Geophysical Research*, *114*, A07217. https://doi.org/10.1029/2009JA014206

Omura, Y., Katoh, Y., & Summers, D. (2008). Theory and simulation of the generation of whistler-mode chorus. *Journal of Geophysical Research*, *113*, A04223. https://doi.org/10.1029/2007JA012622

Omura, Y., & Nunn, D. (2011). Triggering process of whistler mode chorus emissions in the magnetosphere. *Journal of Geophysical Research*, *116*, A05205. https://doi.org/10.1029/2010JA016280

Reeves, G., Spence, H. E., Henderson, M., Morley, S., Friedel, R., Funsten, H., et al. (2013). Electron acceleration in the heart of the Van Allen radiation belts. *Science*, *341*(6149), 991–994.

Santolík, O., Gurnett, D. A., Pickett, J. S., Grimald, S., Décreau, P. M. E., Parrot, M., et al. (2010). Wave particle interactions in the equatorial source region of whistler mode emissions. *Journal of Geophysical Research*, *115*, A00F16. https://doi.org/10.1029/2009JA015218

Santolík, O., Gurnett, D., Pickett, J., Parrot, M., & Cornilleau-Wehrlin, N. (2003). Spatio-temporal structure of storm-time chorus. *Journal of Geophysical Research*, *108*(A7), 1278. https://doi.org/10.1029/2002JA009791

Santolík, O., Kletzing, C. A., Kurth, W. S., Hospodarsky, G. B., & Bounds, S. R. (2014). Fine structure of large-amplitude chorus wave packets. *Geophysical Research Letters*, *41*, 293–299. https://doi.org/10.1002/2013GL058889

Santolík, O., Parrot, M., & Lefeuvre, F. (2003). Singular value decomposition methods for wave propagation analysis. *Radio Science*, *38*(1), 1010. https://doi.org/10.1029/2000RS002523

Sazhin, S., & Hayakawa, M. (1992). Magnetospheric chorus emissions: A review. *Planetary and Space Science*, *40*(5), 681–697. https://doi.org/10.1016/0032-0633(92)90009-D

Spasojevic, M. (2014). Statistical analysis of ground-based chorus observations during geomagnetic storms. *Journal of Geophysical Research: Space Physics*, *119*, 8299–8317. https://doi.org/10.1002/2014JA019975

Summers, D., Ma, C., Meredith, N., Horne, R., Thorne, R., Heynderickx, D., & Anderson, R. (2002). Model of the energization of outer-zone electrons by whistler-mode chorus during the October 9, 1990 geomagnetic storm. *Geophysical Research Letters*, *29*(24), 2174. https://doi.org/10.1029/2002GL016039

Summers, D., Tang, R., & Omura, Y. (2013). Linear and nonlinear growth of magnetospheric whistler mode waves. *Geophysical Monograph Series*, 265–280. https://doi.org.10.1029/2012gm001298

Summers, D., Thorne, R. M., & Xiao, F. (1998). Relativistic theory of wave-particle resonant diffusion with application to electron acceleration in the magnetosphere. *Journal of Geophysical Research*, *103*(A9), 20,487–20,500.

Thorne, R., Li, W., Ni, B., Ma, Q., Bortnik, J., Chen, L., et al. (2013). Rapid local acceleration of relativistic radiation-belt electrons by magnetospheric chorus. *Nature*, *504*(7480), 411–414.

Thorne, R. M., O'Brien, T., Shprits, Y., Summers, D., & Horne, R. B. (2005). Timescale for MeV electron microburst loss during geomagnetic storms. *Journal of Geophysical Research*, *110*, A09202. https://doi.org/10.1029/2004JA010882

Trakhtengerts, V. Y., Demekhov, A. G., Titova, E. E., Kozelov, B. V., Santolik, O., Gurnett, D., & Parrot, M. (2004). Interpretation of Cluster data on chorus emissions using the backward wave oscillator model. *Physics of Plasmas*, *11*(4), 1345–1351. https://doi.org/10.1063/1.1667495

Tsurutani, B. T., & Smith, E. J. (1974). Postmidnight chorus: A substorm phenomenon. *Journal of Geophysical Research*, *79*(1), 118–127.
Wu, S., Denton, R. E., & Li, W. (2013). Effects of cold electron density on the whistler anisotropy instability. *Journal of Geophysical Research: Space Physics*, *118*, 765–773. https://doi.org/10.1029/2012JA018402
Xiao, F., Thorne, R. M., & Summers, D. (1998). Instability of electromagnetic R-mode waves in a relativistic plasma. *Physics of Plasmas*, *5*(7), 2489–2497. https://doi.org/10.1063/1.872932